On-line monitoring of multi-component strain development in a tufting needle using optical fibre Bragg grating sensors

2014 Smart Mater. Struct. 23 075001

(http://iopscience.iop.org/0964-1726/23/7/075001)

OPEN ACCESS
IOP Publishing
Smart Materials and Structures
Smart Mater. Struct. **23** (2014) 075001 (9pp)
doi:10.1088/0964-1726/23/7/075001

On-line monitoring of multi-component strain development in a tufting needle using optical fibre Bragg grating sensors

Edmon Chehura[1], Giuseppe Dell'Anno[2,3], Tristan Huet[2], Stephen Staines[1], Stephen W James[1], Ivana K Partridge[2,4] and Ralph P Tatam[1]

[1] Department of Engineering Photonics, School of Engineering, Cranfield University, Bedfordshire MK43 0AL, Bedford, UK
[2] Composites Centre, Manufacturing and Materials Department, School of Applied Sciences, Cranfield University, Bedfordshire MK43 0AL, Bedford, UK

E-mail: r.p.tatam@cranfield.ac.uk

Received 19 December 2013, revised 18 February 2014
Accepted for publication 20 February 2014
Published 20 May 2014

Abstract

Dynamic loadings induced on a tufting needle during the tufting of dry carbon fibre preform via a commercial robot-controlled tufting head were investigated *in situ* and in real-time using optical fibre Bragg grating (FBG) sensors bonded to the needle shaft. The sensors were configured such that the axial strain and bending moments experienced by the needle could be measured. A study of the influence of thread and thread type on the strain imparted to the needle revealed axial strain profiles which had equivalent trends but different magnitudes. The mean of the maximum axial compression strains measured during the tufting of a 4-ply quasi-isotropic carbon fibre dry preform were $-499 \pm 79\ \mu\varepsilon$, $-463 \pm 51\ \mu\varepsilon$ and $-431 \pm 59\ \mu\varepsilon$ for a needle without thread, with metal wire and with Kevlar® thread, respectively. The needle similarly exhibited bending moments of different magnitude when the different needle feeding configurations were used.

Keywords: optical fibre Bragg gratings, strain measurement, tufting, carbon fibre composite materials

S Online supplementary data available from stacks.iop.org/SMS/23/075001/mmedia

(Some figures may appear in colour only in the online journal)

1. Introduction

Critically stressed structural components for applications in aerospace, automotive, wind energy, marine and civil engineering fields are being manufactured increasingly from polymer matrix/continuous fibre reinforced composites. The typical method used in the production of such composite components involves the manufacture of a preform by stacking unidirectional or cross-ply fibrous layers. These layers can be made out of either fibres pre-impregnated with resin (pre-preg preform), or out of dry fibres (dry preform). Layered pre-pregs can be consolidated and cured (i.e. solidification of the resin by the application of heat) directly after lay-up, while dry preforms must first be infused with a suitable liquid resin before cure. In both cases, the lay-up procedure produces composites with filaments lying in-plane only, and no fibres arranged along the out-of-plane (or Z-) direction. Composites with such fibre architecture are susceptible to

[3] Present address: National Composites Centre, Bristol BS16 7FS, UK.
[4] Present address: Advanced Composites Centre for Innovation and Science, University of Bristol, Bristol BS8 1TR, UK.

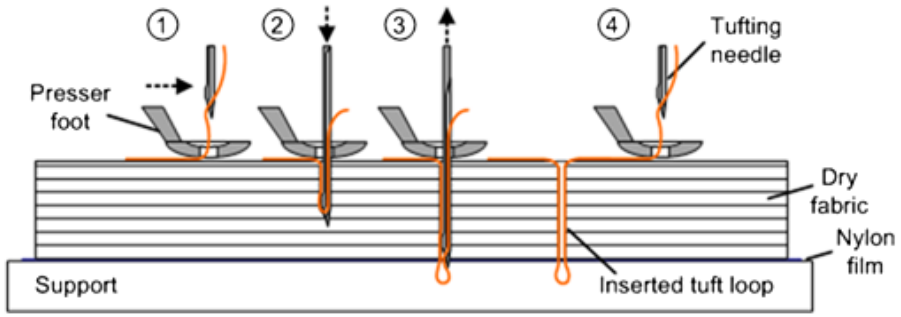

Figure 1. Schematic diagram showing the principle of tufting. The steps in the process are numbered sequentially.

interlaminar delamination upon out-of-plane or impact loading because of the absence of reinforcing fibres bridging adjacent plies. Under specific circumstances, designers may advise the introduction of local reinforcing elements in the Z-direction, so as to increase greatly the resistance to delamination of the component. Several techniques have been developed for inserting Z-reinforcing elements (or '*microfasteners*') through the thickness of the preform, thereby creating three-dimensional (3D) fibre architectures; examples are tufting, stitching or Z-pinning [1–5].

Tufting and stitching are suitable for reinforcing dry preforms prior to liquid resin injection and subsequent cure [1, 3]. Stitching uses two needles to insert and interlock one or more threads into the preform. Tufting, on the other hand, is a modified form of stitching which requires access to the preform from only one side, inserting a single thread with a single needle [2]. The requirement for one sided access is generally seen as an advantage of this process over stitching, as it avoids the creation of significant in-plane-fibre crimp. In cases where Z-direction reinforcement is required for pre-preg lay-ups, one sided Z-pinning is the process of choice. Z-pinning involves the insertion of thin solid carbon fibre based or metallic rods through the thickness of the stack of plies, via an ultrasonic insertion method, which reduces locally the otherwise very high viscosity of the uncured resin in the pre-preg. After insertion, the resin holds the Z-pins in place throughout the remainder of the processing steps. Clearly, the absence of resin in dry preforms means that Z-pin insertion is unlikely to produce a reproducible structure and thus Z-pinning is generally considered unsuitable for use with dry preforms [4, 5]. However, recently developed versions of dry preforms tend to be held together by polymeric binders in the form of powders or veils and in such situations the use of Z-pins may be of benefit.

The present paper concentrates on the technique of tufting and, specifically, on means for the quantification of the strains to which the needles and ultimately the tufting threads themselves are exposed during the tuft insertion process.

Currently available options for commercial tufting threads are Kevlar®, carbon, or glass yarns. Metal wire, being ductile, can be used as an innovative replacement for standard fibrous threads as it could provide potentially novel mechanical properties to the processed composite. During tufting, the needle first penetrates the dry fibre preform, inserting the thread, and then exits along the same path, leaving behind a thread loop (or '*tuft*') that is held in place by friction, as shown in figure 1. A suitable supporting material (typically a sacrificial foam) holds the thread on the underside of the preform, facilitating the formation of the tuft loops.

Experience shows that it is not always possible to tuft a dry preform successfully. Tight weave styles, the use of sizing or binding agents and excessive fibre compaction often make it difficult for the needle to penetrate the preform, resulting in either the tufting machine stopping altogether or, in the worst case, in needle breakage. It becomes necessary to understand better the stresses and strains that the needle undergoes during the tufting process with a view to quantifying the constraints that can limit the use of the technique. Electrical strain gauges, such as resistance foil strain gauges, cannot be used in this application due to their relatively large size compared to the needle dimensions and the curved shape of the needle. This paper presents a technique that monitors on-line and in real-time the multi-component strain experienced by the needle during tufting, measured by multiplexed surface-mounted optical fibre Bragg grating (FBG) sensors.

Optical fibre sensors, and in particular optical fibre Bragg grating (FBG) sensors, are being used increasingly in industrial applications due to the many inherent advantages they possess, such as being generally insensitive to electromagnetic interference, being chemically inert and having resistance to corrosion, which makes them good candidates for deployment in harsh environments. The light weight and small diameter of the optical fibre, generally 50–125 μm for single-mode (SM) optical fibres, make the sensors suitable for both surface-mounted and embedded applications where minimal intrusion is a prerequisite, e.g. in composite materials or aerospace structures.

An FBG is a localized periodic modulation in the otherwise isotropic refractive index of the core of an optical fibre. The FBG couples a forward propagating core mode to a backward propagating core mode at wavelengths of light that satisfy the phase matching condition. The FBG acts as a 'mirror' that reflects, selectively, a narrow wavelength component from an incident broadband light source. The phase matching (or Bragg) condition describes the relationship between the reflected wavelength λ_B, the effective refractive index of the core of the fibre n_{eff} and the grating pitch Λ, as expressed by equation (1) [6].

$$\lambda_B = 2n_{eff}\Lambda. \quad (1)$$

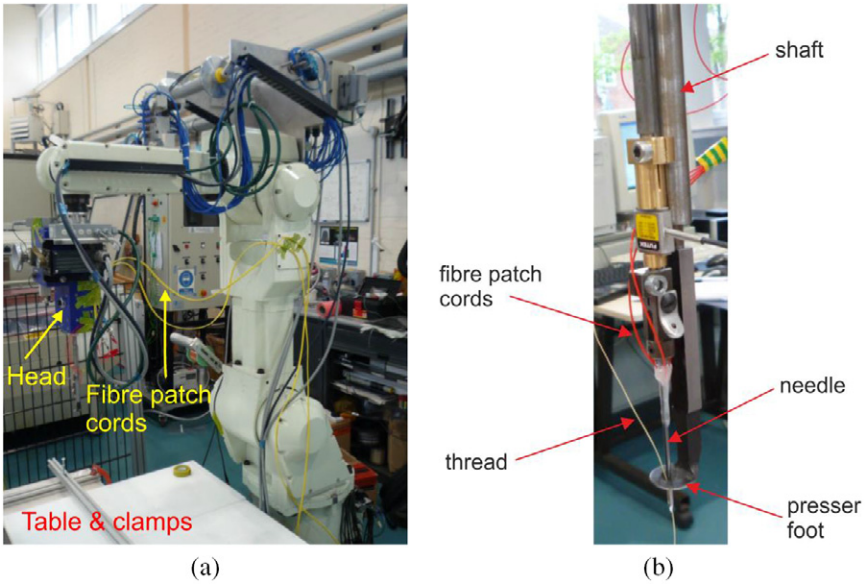

Figure 2. Automated tufting setup showing (a) Kawasaki FN 20 robot arm with tufting head, and (b) detail of the needle and the shaft.

The refractive index grating is created by exposing the core of the optical fibre to a spatially modulated intensity pattern from a laser beam; usually the output from a laser operating in the ultraviolet region of the spectrum. Physical perturbations to the FBG that alter the effective refractive index and/or the grating pitch will cause a concomitant shift in the reflected wavelength. If the FBG is designed to be perturbed by only one particular measurand, then monitoring changes in the wavelength allows one to determine changes in that measurand. FBGs have been applied widely to measure temperature [7, 8], strain [9–13] and pressure [14, 15], while a variety of other measurands can be measured by using specially packaged FBGs [16, 17]. FBG sensors offer many advantages such as localized sensing, high signal to noise ratio and the ability to multiplex a large number of sensors along a single length of optical fibre by fabricating the sensor elements such that each has a distinct centre wavelength. One advantage of employing multiplexed sensors is that their signals can be used to determine multiple components of strain [11, 13].

2. Experimental details

2.1. Tufting instrumentation

A Kawasaki robot system consisting of a 6 axis arm (FS 20N), operated using a program in the Kawasaki proprietary programming language via the dedicated controller software, was used in this work to perform the tufting routines. A commercial tufting head (KSL KL 150) is installed onto the robot arm. The system can be programmed to tuft along different directions, at different insertion angles and at different speeds. The internal mechanism of the tufting head is designed to synchronize the movement of the needle and of the presser foot during tufting. The synchronization ensures that the presser foot starts compressing the preform before the needle starts penetrating it. The presser foot releases its pressure only when the needle has been withdrawn fully from the preform. The thread is not interlocked but is held in place in the preform by frictional forces; hence it is virtually tension free. The dry preform is placed onto the supporting layer and it is mechanically clamped to a 0.9 m by 1.2 m table to stop it from moving during the tufting process. The tufting head is able to tuft at rates between 25 and 500 tufts per minute. The distance between 2 successive tufts (the pitch) can vary between 1 and 10 mm. Figure 2(a) shows the complete robot system, while figure 2(b) provides detail of the mounting, including the needle, shaft and the presser foot.

In the context of this study, three needle feeding configurations were used: tufting was conducted without thread, with a Kevlar® fibrous thread (Tkt40 Nom 250g from Somac) and with a copper wire of 270 μm cross-sectional diameter. These conditions were selected to represent very different and almost extreme loading modes for the needle, with the intention of identifying the effect of the reinforcing medium on the needle strain/stress profiles.

2.2. Fibre Bragg grating sensors

In this work, four wavelength-multiplexed FBG sensors have been used to measure the axial strain and two bending moments experienced by the needle during the tufting process. The sensors, each in a different optical fibre, were multiplexed using the scheme described in [9]. The FBG sensors were fabricated in our laboratories using the phase mask technique [18, 19] at centre wavelengths of 1276, 1286, 1296 and 1304 nm, while the reference FBG was written at 1266 nm. Figure 3 shows the schematic diagram of the system used to interrogate the 4 FBG sensors and a reference FBG which was stabilized at a constant temperature of 25 °C. The configuration shown uses a combination of wavelength-

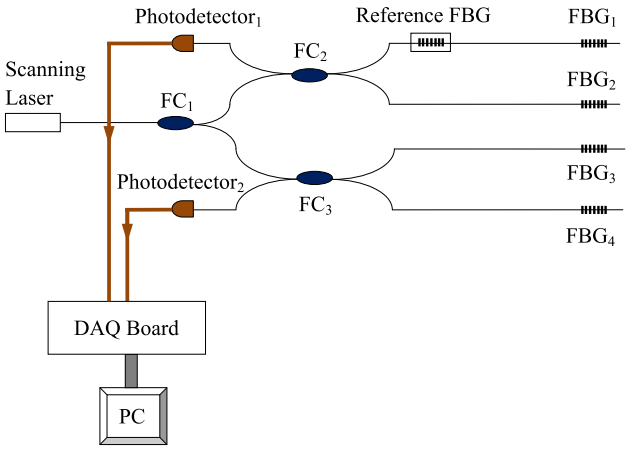

Figure 3. Schematic diagram of the experimental lay-out showing the FBG sensor interrogation system. FC1–FC3: fibre optic directional couplers (50/50 split ratio), FBG1–FBG4: FBGs surfaced-bonded to the needle, DAQ: data acquisition board, PC: personal computer.

and spatial- division multiplexing, as practical constraints mean that it is not possible to instrument the needle using wavelength-division-multiplexed sensors fabricated in a single length of fibre. The scanning laser source has a scan rate of 2.5 kHz and wavelength range of 49 nm centred at 1287 nm (Santec Ltd). The photodetectors (Model 2011, New Focus Inc.) used have a frequency response of 200 kHz (3 dB point). The detector signals were acquired using a 2 GS s^{-1} Digitizer Board (NI PXI-5152) which was installed in an external PXIe chassis (NI PXIe-1073) and recorded simultaneously using a personal computer. The data acquisition program was set up in SCOPE Software (National Instruments) and the sampling rate used was 10 MS s^{-1}, with the full Bragg reflection spectrum being recorded on each scan of the laser source, allowing a data rate of 2.5 kHz, which corresponds to a sweep interval of 400 μs for the laser. The wavelengths of the sensing FBGs were referenced to that of the reference FBG to reduce the noise associated with trigger jitter.

2.3. FBG instrumented needle

Four FBG sensors were attached to the shaft of a tufting needle, 45 mm from the tip of the needle, using cyanoacrylate adhesive. This location was chosen to ensure that the optical fibres remained outside the preform throughout the tufting process, as the maximum stroke of the needle was 40 mm. The dimensions of the needle are approximately 2.1 mm and 100 mm, in diameter and length, respectively. The needle is a steel alloy with an estimated Young's modulus of approximately 225 GPa. The side of the needle facing the tufting direction (front surface) has a groove that leads to a hole at its tip (or needle eye) for the guiding and passage of thread (figure 4(a)). The sensors were aligned with the longitudinal axis of the needle and positioned at 0°, 90°, 180° and 270° around the circumference, where 0° corresponds to the front surface of the tufting needle (figure 4(b)). Plastic sleeves were used to protect the optical fibre downleads (figure 4(a)).

3. Results and discussion

3.1. Thread-less tufting

The preform was made by stacking four plies of carbon fibre unidirectional tape that was coated with a relatively light thermoplastic veil to produce a quasi-isotropic dry preform. The ply orientation in the four layer preform was −45°/90°/45°/0°, from top to bottom. The preform was consolidated on a hot plate maintained at a temperature of 160 °C for 30 min while under vacuum (0.95 bar).

The four layer quasi-isotropic dry preform was then tufted using a needle without thread along a direction aligned with the 0° fibres orientation. The speed of tufting was set at 500 rpm, which is the maximum capability of the tufting unit. The tufting was carried out over a length of 100 mm at a pitch of 2 mm. Figure 5 shows the typical raw strain signals recorded dynamically by each of the 4 FBG sensors. The strain was calculated using equation (2), where $\Delta\lambda_B$ is the measured wavelength shift of the Bragg peak, K_ε is the strain coefficient and $\Delta\varepsilon$ is the calculated strain. A strain coefficient of 0.978 ± 0.002 $\mu\varepsilon$ pm^{-1} was determined by loading known weights onto a freely suspended optical fibre containing an FBG sensor held at constant temperature.

$$\Delta\lambda_B = K_\varepsilon \Delta\varepsilon. \quad (2)$$

Figure 5(a) provides an overview of the signals recorded during the whole tufting procedure, while figures 5(b), (c) present detailed views of the signals generated during three tufts and one tuft, respectively. Positive strain values indicate tension while negative values relate to compression in the needle. A high speed camera (Baumer HXC-13) recorded the movement of the needle in synchrony with the FBG interrogation system, which confirmed the times that the needle entered and exited the preform, indicated by the lines shown in figures 5(b), (c). The line in the figures marking the end-of-stroke of the needle is indicative only. The FBG attached to the front of the needle is within the groove (figure 4) and is therefore the closest to the neutral axis of the needle. The response of the front FBG to tufting loads is thus diminished when compared to that of the back FBG (figure 5(b)). Figure 5(a) shows that the first and final tufts have the longest duration, which is expected as the robot head is programmed to accelerate and decelerate progressively at the start and end of the tufting routine. Figures 5(b), (c) show that measured strain is zero or near zero when the needle is completely outside the preform. The influence of the groove on the mechanical behaviour of the needle was investigated by a three-point bending test, which estimated flexural moduli of 90 GPa and 300 GPa in the back–front plane and the left–right plane, respectively.

The strains measured by the four sensors in figure 5 have contributions from axial and bend strains. The strain components can be separated from each other by using the beam bending theory. The general expression for axial stress, σ_x, in a homogeneous beam that has an asymmetrical cross-section is given by equation (3), for a coordinate system with the origin at the neutral axis [20].

$$\sigma_x(y,z) = -\frac{M_z J_{yy} + M_y J_{yz}}{J_{yy}J_{zz} - J_{yz}^2} y + \frac{M_y J_{zz} + M_z J_{yz}}{J_{yy}J_{zz} - J_{yz}^2} z \quad (3)$$

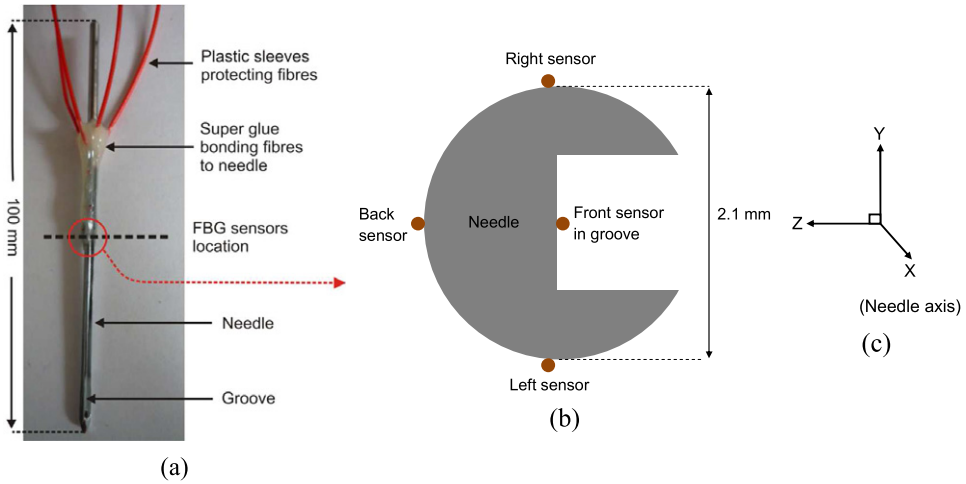

Figure 4. (a) Tufting needle showing bonded optical fibres containing the 4 FBG sensors and (b) cross-section of the needle showing the locations of the attached FBG sensors. The cross-section is taken from the encircled region of the needle (red circle) where the sensors are bonded. (c) An insert of the coordinate system in which the x-axis is the needle axis, y-axis is the left/right plane and z-axis is the back/front plane.

M_y and M_z are the bending moments about the y and z centroid axes, J_{yy} and J_{zz} are the second moments of area about the y and z axes, while J_{yz} is the product of moments of area. The needle is equivalent to a beam that consists of a cross-section with an axis of symmetry, in this case the z axis defined in figure 6. It can be shown therefore that the product of moments of area about two orthogonal axes is zero, i.e. $J_{yz} = 0$ *in* equation (3), which leads to equation (4). This means there is no coupling between the two bending moments described in equation (3).

$$\sigma_x(y, z) = -\frac{M_z}{J_{zz}}y + \frac{M_y}{J_{yy}}z. \tag{4}$$

When the stresses at the FBG sensor locations in figure 6, i.e. σ_L, σ_R and σ_B, at the left, right and back of the needle, respectively, are substituted together with the coordinates at these locations into equation (4), equations (5) and (6) are obtained. The axial stress in the needle, σ_a, is given by the sum of the direct axial stress and the axial stress due to the bending moments (equation (7)). Direct axial stress can be considered as the sum and average of the stresses σ_L, σ_R and σ_B. It can be shown that the axial stress is given by equation (8) while equation (9) represents the offset of the centroid of the grooved needle from that of a needle of the same diameter without a groove.

$$M_z = J_{zz}\frac{(\sigma_L - \sigma_R)}{2r} \tag{5}$$

$$M_y = J_{yy}\frac{[2\sigma_B - (\sigma_L + \sigma_R)]}{2r} \tag{6}$$

$$\sigma_a = \sigma_a^{direct} + \sigma_a^{Bend} \tag{7}$$

$$\sigma_a = \frac{8\sigma_B - (\sigma_L + \sigma_B)}{6} + 3C\frac{[(\sigma_L + \sigma_R) - 2\sigma_B]}{2r} \tag{8}$$

$$C = G_N - G_O. \tag{9}$$

The symbols r, G_N and G_O represent the radius of the needle, the centroid of the needle and the centroid for a needle without a groove, respectively, with $r = 1088\ \mu$m and $C = 185.17\ \mu$m. The stresses σ_L, σ_R and σ_B, are calculated from the strains ε_L, ε_R and ε_B, respectively, using equation (10).

$$\sigma_i = E\varepsilon_i. \tag{10}$$

The subscript $i = $ L, R, or B, where L, R and B represent left, right and back, respectively. E is the Young's modulus of the needle.

The centroid of the needle is determined using the 'composite area theorem' by dividing the cross-sectional shape of the needle into several subsections, shown as a, b, c, d and e, in figure 6. The theorem states that the distance from an arbitrary axis to the centroid of an area made up of several subareas is the sum of the subareas times the distance to their individual centroids, divided by the sum of the subareas. The moment of inertia of a composite area of the needle is then determined by using the parallel axis theorem [21], to obtain the values of J_{zz} and J_{yy} to be used in equations (5) and (6). The calculated values of J_{zz} and J_{yy} were 1.6161×10^{-6} m^4 and 2.0202×10^{-6} m^4, respectively.

Figure 7 shows the axial strain and bending moments which were evaluated from the raw strains in figure 5 using equations (5)–(10). During tufting, the needle penetrates the preform to its maximum depth in the supporting substrate before being extracted from the substrate through the preform to the outside again. The time the needle takes to penetrate to its maximum depth, 28 ms, is equal to the time the needle takes to be extracted from the preform from its maximum depth (figure 7(c)). The number of wavelength shift measurements made during the 56 ms downward/upward stroke of the needle is 140, which corresponds to a time interval of 400 μs for the FBG spectral acquisition. The time the needle is translating outside the preform to the next tuft is 70 ms (figure 7(c)).

Data recorded during the part of the tuft cycle during which the needle is embedded in the preform shows the needle experiencing a predominantly compressive axial strain

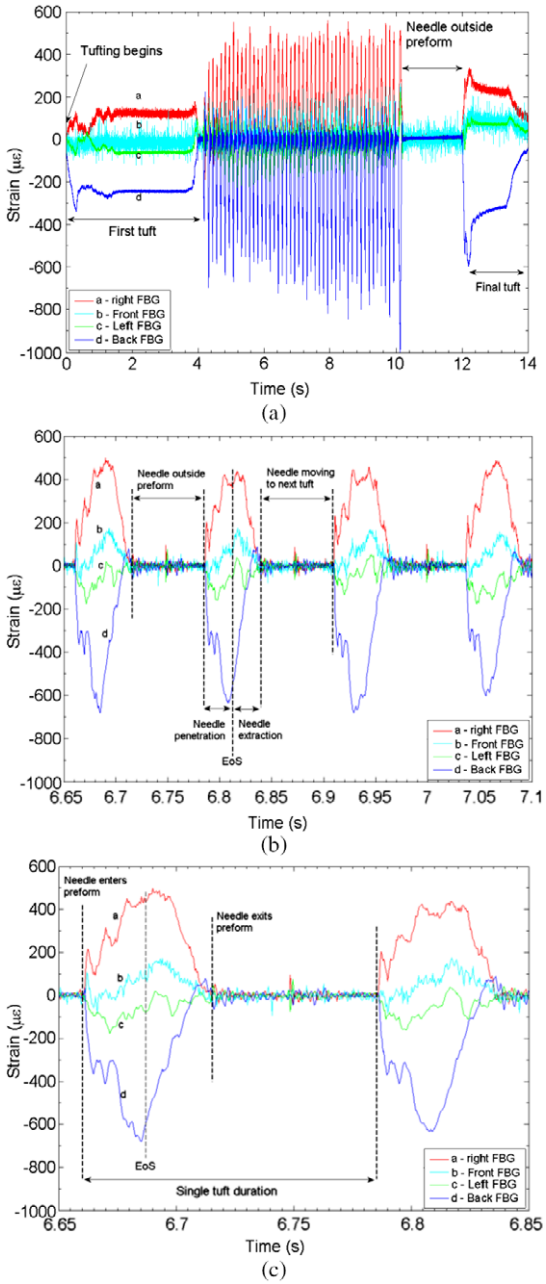

Figure 5. Strain signals from the four individual FBG sensors showing (a) an entire tuft process over a whole length of preform, (b) ∼3 tuft periods and (c) ∼1 tuft period. A 4 layer quasi-isotropic preform was tufted by a thread-less needle at a tufting speed of 500 rpm. EoS: end of stroke.

(figures 7(b), (c)). As the needle penetrates into the preform, it pushes against the fabric, which causes the compression strain to increase (figures 7(b), (c)). As the needle is extracted from the preform, the compressive load decreases with a reduction in the calculated compression strain, (figures 7(b), (c)). The average of the maximum recorded compressive axial strain over all tufting cycles along a whole length of preform was $\sim -499 \pm 79\ \mu\varepsilon$ (figures 7(b), (c)). When the needle is outside the preform, the axial strain is approximately zero.

The bending moment measured in the left–right plane of the needle is predominantly negative, with an average

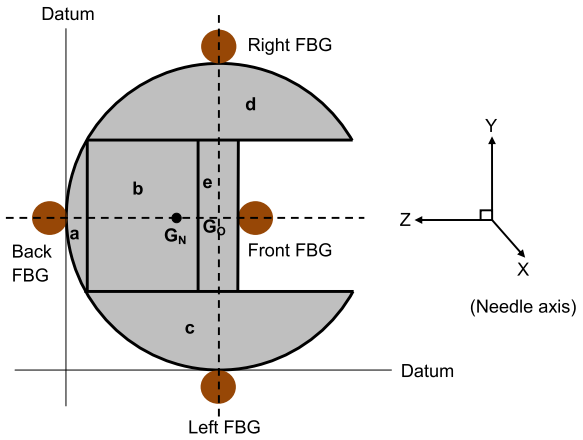

Figure 6. Needle cross-section showing the subdivisions into 5 sections (a, b, c, d, and e) which were used to determine the centroid G_N, the neutral axis and the moment of inertia. The centroid for a needle without the groove would be G_O. The coordinate system used is denoted by the insert.

maximum of $\sim -95 \pm 20$ kN m when the needle is within the preform (figures 7(b), (c)). This indicates that the needle was bending towards the left during tufting. Such bending will occur when the needle is attached to the robot head with a slight misalignment, such that the needle leant toward the left before each insertion. When the needle is outside the preform, the bending moment measured in the left–right plane is approximately zero, as expected. The mean of the bending moment measured in the back–front plane of the needle is -262 ± 51 kN m when the needle is embedded within the preform (figures 7(b), (c)). This suggests that the needle was bending away from the direction of travel of the robot head (i.e. backwards). Such bending moment is to be expected as the robot head moves forward continually, even while the needle is fully inserted into the preform. As the needle penetrates the preform, the bending moment in the back–front plane exhibits 4 clearly defined troughs, labelled p1–p4 in figure 7(c). The 4 troughs are characteristic of the penetration of the needle through each of the 4 layers/plies of the quasi-isotropic preform. In separate experiments, conducted with sixteen-ply preforms (but not reported here), the correspondence between the number of troughs in the bending moment profile and the number of plies was confirmed.

3.2. Tufting with thread

The influence of thread and thread type on tufting was investigated. The experiment described in section 3.1, in which a four layer quasi-isotropic medium was tufted without thread, was repeated first with metal wire and then with Kevlar® thread. The conditions under which the experiments were conducted were the same as per the thread-less setup.

Figure 8 compares the axial strain measured in the needle from the three different experiments employing different needle feeding conditions. Axial strains exhibited by the needle when metal wire and Kevlar® thread were used follow the trend of the axial strain recorded for a thread-less needle, as described by figures 8(b), (c) (also figure 7). The mean

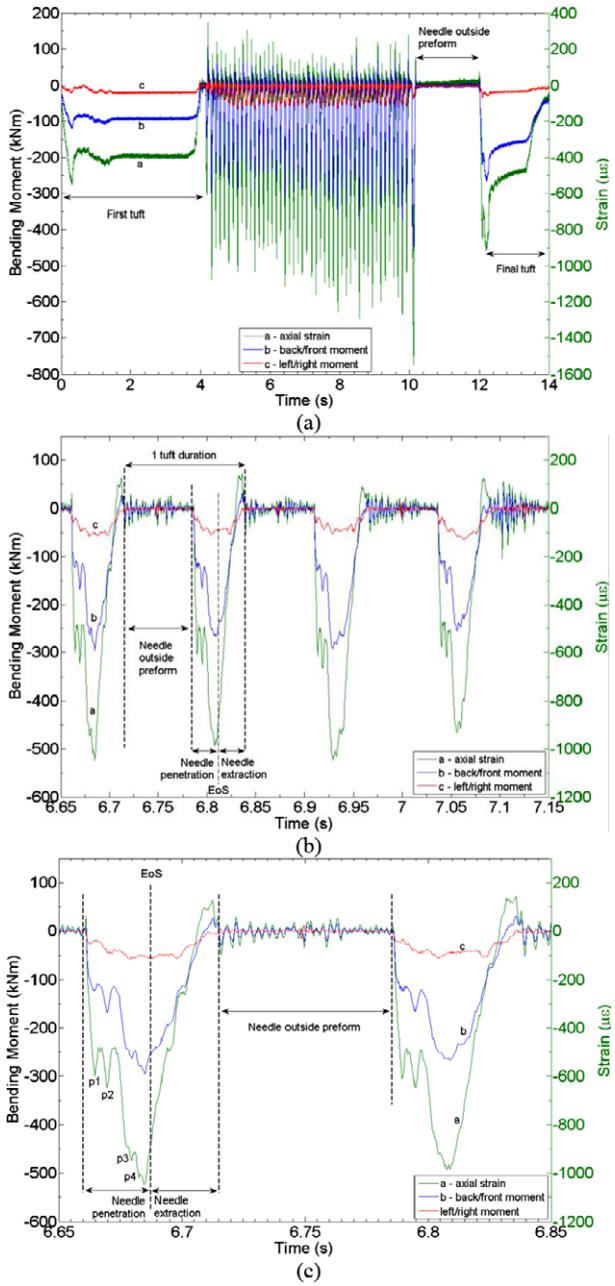

Figure 7. Axial strain and bending moments evaluated from 4 FBG signals of figure 5: (a) an entire tuft process over the whole length of preform, (b) ∼3 tuft periods and (c) ∼1 tuft period. A 4 layer quasi-isotropic preform was tufted by a thread-less needle at a tufting speed of 500 rpm. p1–p4: troughs, EoS: end of stroke.

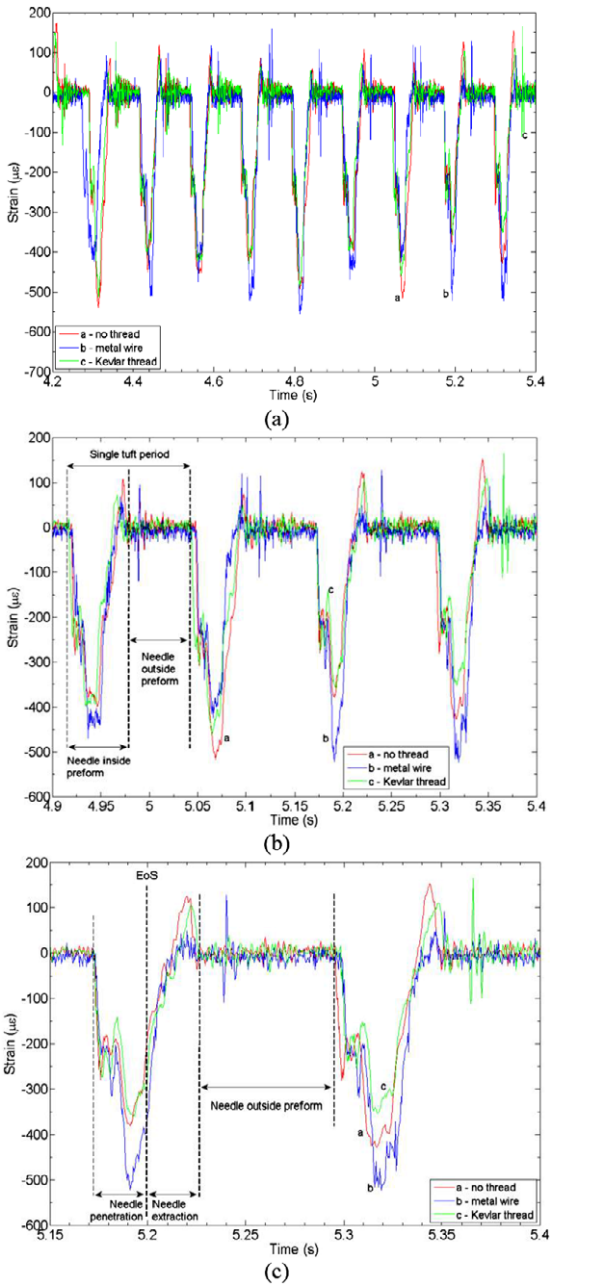

Figure 8. Axial strain in the needle evaluated from the signals measured by 4 FBG sensors showing (a) several tuft periods, (b) ∼3 tuft periods and (c) ∼1 tuft period. A 4 layer quasi-isotropic preform was tufted at a speed of 500 rpm by a needle without thread, with metal wire and Kevlar® thread. EoS: end of stroke.

of the maximum compressive axial strains recorded were $-499 \pm 79\ \mu\varepsilon$, $-463 \pm 51\ \mu\varepsilon$ and $-431 \pm 59\ \mu\varepsilon$ for a needle without thread, with metal wire and with Kevlar® thread, respectively (figure 8). The mean was obtained from 10 tuft cycles of the needle. The compressive nature of the axial strain is to be expected, as discussed in section 3.1. In general, the three strain traces reveal corresponding features, while the trace obtained when using the metal wire is characterized by some high frequency features (figure 8(c)). The high frequency features might arise from additional friction imposed on the needle by the metal wire, which is stiffer than Kevlar® thread.

Figure 9 compares bending moments measured in the left–right plane of the needle during the experiments described above. Bending moments for a needle with thread showed that the needle was bending predominantly leftwards, as was the thread-less needle (figures 9(b), (c)) discussed in section 3.1. The mean of the maximum bending moments recorded from all three experiments employing different needle feeding configurations were -95 ± 20 kN m, -64 ± 13 kN m and -158 ± 32 kN m for the needle without thread, with metal wire and with Kevlar® thread, respectively (figure 9). The data shows that the bending moment is influenced by the presence of thread or by the thread type. While the same

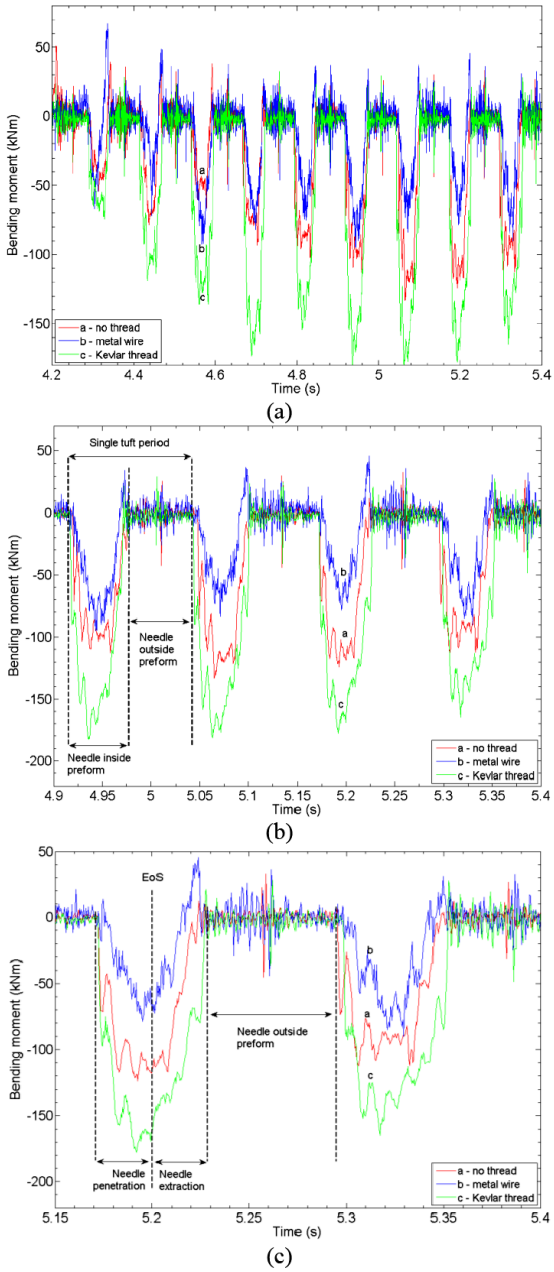

Figure 9. Bending moment in the left–right plane of the needle evaluated from the signals measured by 4 FBG sensors showing (a) several tuft periods, (b) ∼3 tuft periods and (c) ∼1 tuft period. A 4 layer quasi-isotropic preform was tufted at a speed of 500 rpm by a needle without thread, with metal wire and Kevlar® thread. EoS: end of stroke.

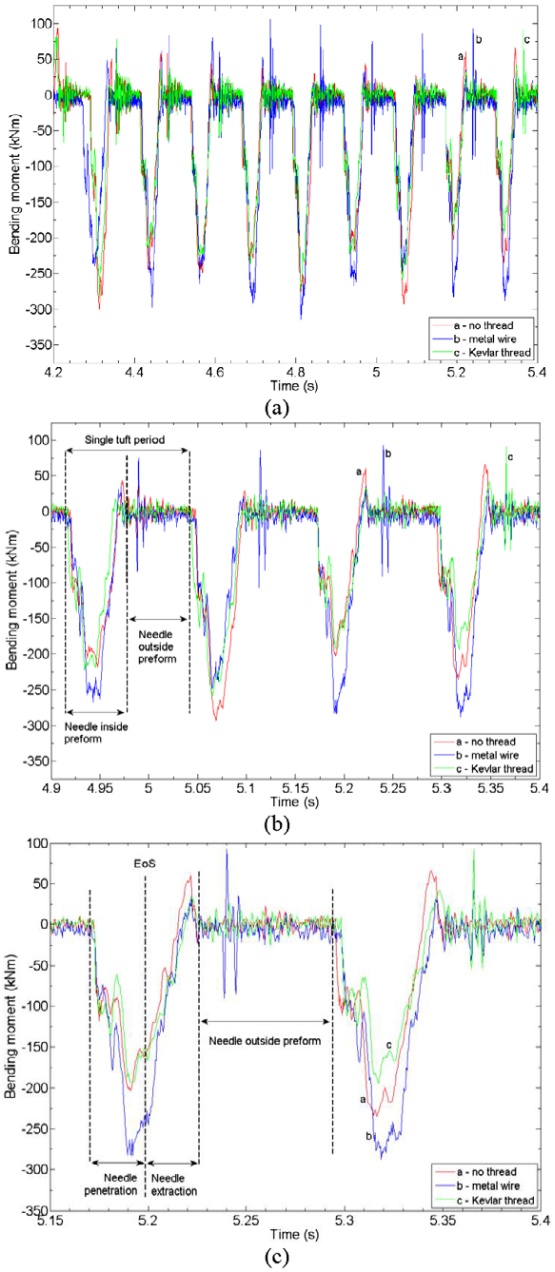

Figure 10. Bending moment in the back–front plane of the needle evaluated from the signals measured by 4 FBG sensors showing (a) several tuft periods, (b) ∼3 tuft periods and (c) ∼1 tuft period. A 4 layer quasi-isotropic preform was tufted at a speed of 500 rpm by a needle without thread, with metal wire and Kevlar® thread. EoS: end of stroke.

trend is followed by the three bending moment curves, the curve for metal wire is also characterized by high frequency features (figure 9(c)) which might be caused by additional friction imposed by the rather stiffer metal wire (see axial strain above). The bending moment measured when the needle was outside of the preform and was in translation to the next tuft position is characterized by damped oscillations for the cases of needle with Kevlar® thread and wire, while there are no significant oscillations for a thread-less needle, apart from noise (figures 9(b), (c)). Generally, the needle exhibited bending moment oscillations with larger amplitude when the metal wire was used, compared to that observed for Kevlar®. The oscillations are centred at 0 kN m. The bending moment measured in the left–right plane of the needle confirms that the presence of thread or wire on the needle influences the strain response even when the needle is outside the preform (figures 9(b), (c)).

Bending moments measured in the back–front plane of the needle from the three experiments described above are compared in figure 10. The bending moments recorded when the needle was equipped with threads were predominantly negative in the part of the tuft cycle during which the needle was embedded within the preform (figures 10(b), (c)), as for thread-less case (section 3.1). The needle was therefore

bending backwards from the direction of travel of the robot head (section 3.1). The mean of the maximum bending moments recorded during each of the three experiments were -262 ± 51 kN m, -253 ± 21 kN m and -220 ± 39 kN m for the needle without thread, with metal wire and with Kevlar® thread, respectively (figure 10(a)). The bending moment curves exhibit a common trend (figure 10(c)). For a time of ∼9 ms, just before the needle exits the preform (figure 10(c)), the bending moment in the back–front plane becomes positive before it approaches zero rapidly at the point of exit of the needle from the preform (figures 10(b), (c)). The recorded bending moment in the part of the tuft cycle during which the needle was outside of the preform is characterized by damped oscillations, regardless of the needle having or not having a thread (figures 10(a), (c)). The bending moment oscillations are centred at 0 kN m. The bending moment response of the needle is therefore influenced by the presence of thread regardless of whether the needle is within or outside of the preform. A spike in the bending moment recorded for a needle equipped with metal wire is observed when the needle is outside the preform and is translating to start another tuft. The spikes appear at approximately the same points in each tuft cycle (figure 10(b)). Metal wire is much stiffer than the fibrous Kevlar® thread and thus it is likely that sudden resistance or slippage in the metal wire, on the bobbin for example, might impose sudden changes to the frictional forces imparted onto the needle, explaining the presence of the spikes in the bending moment.

Supplementary data is available at stacks.iop.org/SMS/23/075001/mmedia.

4. Conclusion

Multiplexed FBG sensors have been employed successfully to measure multiple components of dynamic strain imparted into the needle during tufting of dry carbon fibre preforms. This new technique is capable of providing significant new insight into the tufting process. It can be used as a research tool to provide better understanding of the interactions between the tufting tool and the preform; this may ultimately lead to an informed control of this particular new composites manufacturing process. This is a clear example of an application in which the small dimensions of the optical fibre facilitate measurements that are not possible using other technologies.

Acknowledgments

This work was supported by the European Union Framework 7 Programme, Advanced Integrated Tailcone (ADVITAC) [22] and by the Engineering and Physical Sciences Research Council (UK) via a Platform Grant, number EP/H02252X/1.

References

[1] Dell'Anno G, Cartié D D R, Partridge I K and Rezai A 2007 Exploring mechanical property balance in tufted carbon fabric/epoxy composites *Composites* A **38** 2366–73

[2] Treiber J W G 2011 Performance of tufted carbon fibre/epoxy composites *PhD Thesis* Cranfield University (http://dspace.lib.cranfield.ac.uk/handle/1826/5531)

[3] Dransfield K, Baillie C and Mai Y 1994 Improving the delamination resistance of CFRP by stitching—a review *Compos. Sci. Technol.* **50** 305–17

[4] Mouritz A P and Cox B N 2010 A mechanistic interpretation of the comparative in-plane mechanical properties of 3D woven stitched and pinned composites *Composites* A **41** 709–28

[5] Cartié D D R, Dell'Anno G, Poulin E and Partridge I K 2006 3D reinforcement of stiffener-to-skin T-joints by *Z*-pinning and tufting *Eng. Fract. Mech.* **73** 2532–40

[6] Hill K O, Fuji Y, Johnson D C and Kawasaki B S 1978 Photosensitivity in optical fiber waveguide: application to reflection filter fabrication *Appl. Phys. Lett.* **32** 647–9

[7] Rao Y-J, Webb D J, Jackson D A, Zhang L and Bennion I 1997 In-fiber Bragg-grating temperature sensor system for medical applications *J. Lightwave Technol.* **15** 779–85

[8] James S W, Dockney M L and Tatam R P 1996 Simultaneous independent temperature and strain measurement using in-fibre Bragg grating sensors *Electron. Lett.* **32** 1133–4

[9] Kersey A D, Berkoff T A and Morey W W 1993 Multiplexed fiber Bragg grating strain-sensor system with a fiber Fabry–Perot wavelength filter *Opt. Lett.* **18** 1370–172

[10] Ling H, Lau K, Cheng L and Chow K 2005 Embedded fibre Bragg grating sensors for non-uniform strain sensing in composite structures *Meas. Sci. Technol.* **16** 2415–24

[11] Chehura E, Skordos A A, Ye C-C, James S W, Partridge I K and Tatam R P 2005 Strain development in curing epoxy resin and glass fibre/epoxy composites monitored by fibre Bragg grating sensors in birefringent optical fibre *Smart Mater. Struct.* **14** 354–62

[12] James S W, Tatam R P, Fuller S R and Crompton C 1999 Monitoring transient strains on a gun barrel using fibre Bragg-grating sensors *Meas. Sci. Technol.* **10** 63–7

[13] Chehura E, Buggy S J, James S W, Johnstone A, Lakrimi M, Domptail F, Twin A and Tatam R P 2011 Multi-component strain development in superconducting magnet coils monitored using fibre Bragg grating sensors fabricated in highly linearly birefringent fibre *Smart Mater. Struct.* **20** 125004

[14] Takahashi N, Hirose A and Takahashi S 1997 Underwater acoustic sensor with fiber Bragg grating *Opt. Rev.* **4** 691–4

[15] Xu M G, Geiger H and Dakin J P 1996 Fibre grating pressure sensor with enhanced sensitivity using a glass-bubble housing *Electron. Lett.* **32** 128–9

[16] Correia R, Chehura E, Li J, James S W and Tatam R P 2010 Enhanced sensitivity fibre Bragg grating (FBG) load sensor *Meas. Sci. Technol.* **21** 094006

[17] Mokhtar M R, Sun T and Grattan K T V 2012 Bragg grating packages with nonuniform dimensions for strain and temperature sensing *J. Sensors* **12** 139–44

[18] Dockney M L, James S W and Tatam R P 1996 Fibre Bragg gratings fabricated using a wavelength tuneable laser source and a phase mask based interferometer *Meas. Sci. Technol.* **7** 445–8

[19] Hill K O, Malo B, Bilodeau F, Johnson D C and Albert J 1993 Bragg gratings fabricated in monomode photosensitive optical fibre by UV exposure through a phase mask *Appl. Phys. Lett.* **62** 1035–7

[20] Cook R D and Young W C 1985 *Advanced Mechanics of Materials* (New York: Macmillan)

[21] Benham P P, Crawford R J and Armstrong C G 1996 *Mechanics of Engineering Materials* 2nd edn (Englewood Cliffs, NJ: Prentice-Hall)

[22] www.advitac.eu/